# Estimation of Radio Refractivity Structure Using Matched-Field Array Processing

Peter Gerstoft, Donald F. Gingras, *Member, IEEE*, L. Ted Rogers, and William S. Hodgkiss, *Member, IEEE*

***Abstract*—In coastal regions the presence of the marine boundary layer can significantly affect RF propagation. The relatively high specific humidity of the underlying "marine layer" creates elevated trapping layers in the radio refractivity structure. While direct sensing techniques provide good data, they are limited in their temporal and spatial scope. There is a need for assessing the three-dimensional (3-D) time-varying refractivity structure. Recently published results (Gingras *et al.* [1]) indicate that matched-field processing methods hold promise for remotely sensing the refractive profile structure between an emitter and receive array. This paper is aimed at precisely quantifying the performance one can expect with matched-field processing methods for remote sensing of the refractivity structure using signal strength measurements from a single emitter to an array of radio receivers. The performance is determined via simulation and is evaluated as a function of: 1) the aperture of the receive array; 2) the refractivity profile model; and 3) the objective function used in the optimization. Refractivity profile estimation results are provided for a surface-based duct example, an elevated duct example, and a sequence of time-varying refractivity profiles. The refractivity profiles used were based on radiosonde measurements collected off the coast of southern California.**

***Index Terms*—Antenna arrays, electromagnetic propagation in nonhomogeneous media, refractivity estimation, signal processing, UHF radio propagation.**

## I. Introduction

THE ability to predict variation of the received signal level in the troposphere at microwave frequencies due to terrain and refractive index effects is an important aspect of predicting the performance of modern radar and communications systems. Currently, there are a number of well-established propagation prediction models, c.f. [2]–[5]. The major issue with respect to propagation prediction, especially in coastal environments, is knowledge of the atmospheric parameters that determine the refractivity structure as a function of time and space. Efforts are underway to improve the quality of the refractivity inputs, including improving meso-scale weather models and developing or improving direct and remote sensing of the refractivity structure (a survey can be found in [6]).

Two important and variable atmospheric features found in the coastal region are the surface-layer evaporation duct and the elevated refractive layers at the top of the marine boundary layer. Both are caused by vertical gradients of temperature (increase) and humidity (decrease). The evaporation duct is surface-based and is persistent over ocean areas because of the rapid decrease of moisture immediately above the surface. Evaporation ducts [Fig. 1(a)] are small (typically less than 30 m high), but have a substantial effect on the propagation of radio waves above 3 GHz.

Elevated trapping layers [either surface-based Fig. 1(b) or elevated Fig. 1(c)] are prevalent in coastal regions. Ducts occur when a stable atmospheric condition results in a temperature inversion and a sufficient amount of water vapor is trapped below that inversion. This condition causes a rapid decrease in the refractive index with increasing height leading to waveguide-like trapping. Although temperature inversions are often referred to as the characterizing feature of elevated ducts, it is the humidity gradient that dominates radio refractivity. A surface-based duct is created when the $M$ value at the top of the trapping layer is less than the surface $M$ value. In the elevated duct case, it is necessary that the $M$ value at the top of the trapping layer be greater than the $M$ value at some height below the trapping layer. For both ducts the propagating radio wave is trapped between the two bounds, creating an interference pattern suitable for inversion.

Quantifying the refractivity structure in time and space is a difficult problem especially in the coastal zone where the sharp contrast between land and sea strongly contributes to both temporal and spatial variability. Sensing of radio refractivity has historically been accomplished with direct sensing techniques such as radiosondes, microwave refractometers, and evaporation duct sensors. In comparison to the large geographic regions over which it is desired to know the refractivity structure, direct sensors provide only a sparse sampling in time and space. Remote sensing has the potential to provide path-integrated refractivity estimates in near real time. Neither direct or remote sensing methods will provide the total picture; a data fusion approach that combines the information from direct and remote sensing along with the results of numerical weather prediction models is required.

A promising method for remote sensing of the refractivity structure is based on inference from measurements of signal strength. Hitney demonstrated the capability to assess the base height of the trapping layer from observations of radio signal strength [7]. Boyer *et al.* estimated refractivity from measurements with substantial diversity in both height and frequency [8]. Tabrikian *et al.* combined prior statistics of refractivity with propagation measurements for inferring refractivity [9]. Rogers inferred refractivity parameters from magnitude measurements at a single point with limited frequency diversity [10]. Anderson

Manuscript received April 13, 1998; revised October 12, 1999. This work was supported by the Office of Naval Research.

P. Gerstoft and W. S. Hodgkiss are with the Marine Physical Laboratory, University of California, San Diego, CA 92093-0701 USA.

D. F. Gingras and L. T. Rogers are with the Propagation Division, Space and Naval Warfare Systems Center, San Diego, CA 92152-7385 USA.

Publisher Item Identifier S 0018-926X(00)02462-5.

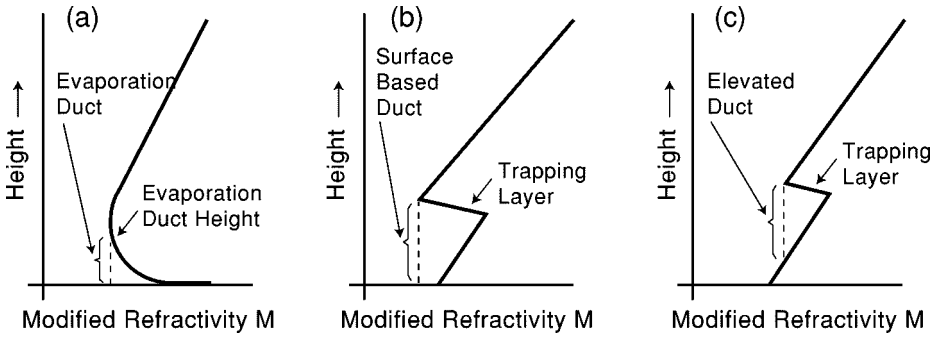


Fig. 1. Modified refractivity $M$ versus height. (a) Evaporation duct. (b) Surface-based duct. (c) Elevated duct. The modified refractivity is the refractivity multiplied with $10^6$ and corrected for the curvature of the earth.

inferred vertical refractivity of the lower atmosphere based on ground-based measurements of global positioning system (GPS) signals [11].

The estimation or inference of atmospheric refractivity structure from radio signal strength measurements is an inverse problem. Matched-field processing methods represent one approach for solving inverse problems through the use of extensive forward modeling. The basic method of electromagnetic matched-field processing and the related genetic algorithms (GA) based global optimization procedures are discussed in [1]. It was also shown, using a single simulation example, that it may be possible to jointly estimate the location of an RF emitter and refractivity parameters using signal strength measurements.

The present paper is a sequel to [1] in that it is directed toward quantifying the performance for matched-field processing methods for remotely sensing refractivity structure. Synthetic signal strength measurements from an emitter to an array of radio receivers are generated for a variety of measured refractivity profiles. The synthetic measurements are used to assess performance of the matched-field methods. The refractivity profile estimation performance is analyzed as a function of: 1) aperture of receiver array; 2) refractivity profile models; and 3) a number of objective functions. Results are provided for a surface-based duct example, an elevated duct example, and a time series containing a wide range of profile types.

The emphasis here is to bound the performance of a real system. The effect of environmental mismatch is not considered and the same propagation model is used for generating both the synthetic signal and the replica vectors.

Actual refractivity profiles were used in the simulations and they were based on radiosonde measurements collected off the coast of southern California in an experiment aimed at characterizing the variability of coastal atmospheric refractivity (VOCAR). In Section II, the geometry and refractivity data obtained during the VOCAR experiment are discussed. Then, Section III presents the matched-field processing methods used for refractivity profile estimation. In Section IV, the simulation approach and results are discussed. Finally, conclusions of this work are summarized in Section V.

## II. VOCAR Experimental Data

Meteorological data and path geometries used in the simulations of Section IV were taken from the variability of coastal atmospheric refractivity (VOCAR) experiment [12]. The meteorology is discussed in [13]. The VOCAR experiment was conducted during the period June 1–September 7, 1993 in the southern California bight. During VOCAR, transmission measurements at VHF and UHF frequencies were recorded on paths from San Clemente Island to Point Mugu (Path A) and from San Clemente Island to San Diego (Path B), as shown in Fig. 2. Three continuous wave (CW) transmitting systems at 143.09, 262.85, and 374.95 MHz were installed at the northwest end of San Clemente Island. Receiving systems were located both at Point Mugu and San Diego. Table I provides the physical dimensions for both VOCAR paths.

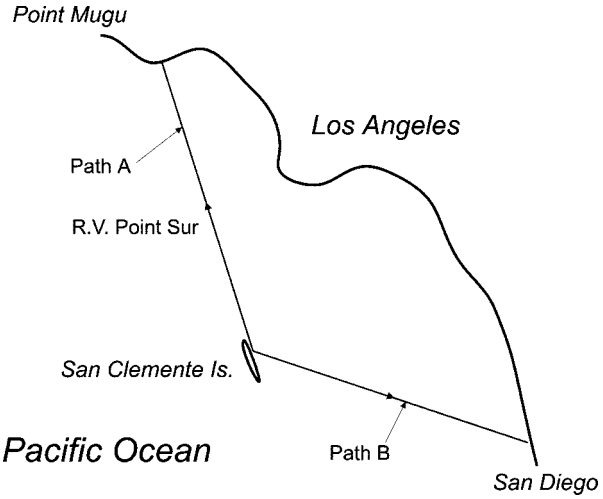


Fig. 2. Depiction of southern California bight showing the two transmission paths used during VOCAR.

TABLE I
VOCAR Geometries

| Parameter | Path A | Path B |
|---|---|---|
| Path length (km) | 132.6 | 127.2 |
| Transmitter height (m) | 18.4 | 16.6 |
| Receiver height (m) | 30.5 | 30.5 |

Fig. 3 shows two refractivity profiles, corresponding to a typical surface-based duct and elevated duct, selected from the large number of refractivity profiles collected during VOCAR. On the right side of each refractivity profile, the corresponding coverage diagrams computed at a frequency of 375 MHz for

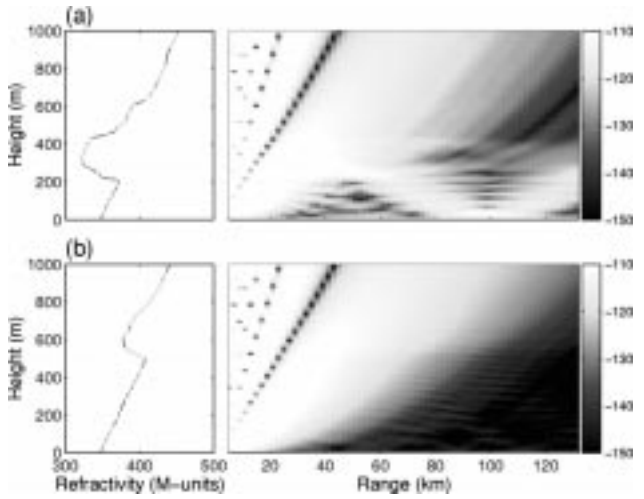


Fig. 3. Refractivity profile and corresponding coverage diagram at 375 MHz for (a) surface-based duct and (b) elevated duct. The coverage diagrams show propagation loss in decibels versus range and height for a source of unit strength. The propagation loss was computed by the propagation model TPEM [4].

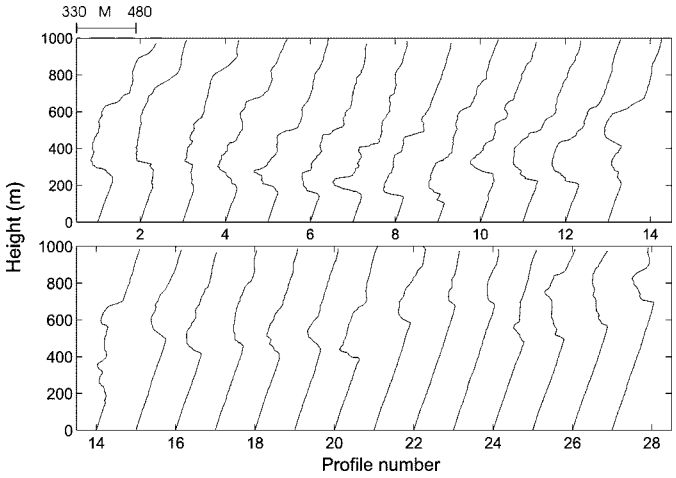


Fig. 4. Time series of modified refractivity profiles taken by the *R/V Point Sur* during the VOCAR intensive operation period.

an emitter height of 18.4 m are presented. The surface-based duct coverage diagram shows a duct extending from the surface to about 300 m and several reflections within the duct. It is expected that this field information, as observed at the receive array, can be used to estimate the refractivity profile. For the elevated duct example, a duct exists between 200 and 600 m. Since the emitter isnot intheduct, littleenergyistrapped. Thus, there is little energy at the receive array location that can be used for profile estimation purposes.

During a two week intensive operation period from August 23 to September 2, 1993, "high-resolution" radiosondes were launched at numerous locations in the southern California bight, including 43 from San Clemente Island, 27 from the *R/V Point Sur* (located midway between San Clemente Island and Point Mugu on Path A), and another 43 at Point Mugu. Fig. 4 illustrates a time series of modified refractivity profiles calculated from the radiosondes launched from the R/V Point Sur over a 4.5 day period during the above period (one every 4 h). The surface-based duct and elevated duct examples and the R/V Point Sur refractivity profile time series along with the VOCAR Path A geometry are used in Section IV as the basis for the simulation analysis.

## III. Refractivity Estimation

Cast as an environmental inversion problem, matched-field processing involves the following: an environmental model parameterized by a vector of uncertain parameters $\boldsymbol{m}$, an electromagnetic propagation model for calculating the predicted replica field $\boldsymbol{p}(\boldsymbol{m})$, an objective function $\phi(\boldsymbol{m})$ that calculates the match between the predicted field $\boldsymbol{p}(\boldsymbol{m})$ and observed field $\boldsymbol{q}(\boldsymbol{m})$, and an efficient search method for searching the model parameter space. Here, the optimization is carried out by GA as implemented in [16]. For generation of the electromagnetic field $\boldsymbol{p}(\boldsymbol{m})$, the parabolic equation method as implemented in the terrain parabolic equation model (TPEM) [4] was used.

### A. Refractivity Models

An actual refractivity profile calculated from radiosonde measurements (modified refractivity versus height) may contain a large number of values. In order to estimate a profile, a compact representation or parametric model must be used by the estimation process. One such model is the trilinear profile model reported in [10], see Fig. 5. The trilinear model is exactly determined by seven independent parameters. Those parameters can be the value of modified refractivity at the surface $M(0)$ (essentially an offset), the slope in the mixed layer, the inversion base height $z_I$, the thickness of the inversion $dz$, the $M$-deficit $dM = M(z_I + dz) - M(z_I)$, which is the change in refractivity across the inversion and the slope and length of the segment above the inversion.

Four of the seven parameters are fixed in this analysis; those parameters and the reasons for choosing them are as follows.

1) For the field calculated at a single frequency, an arbitrary constant can be subtracted from the $M$-profile without affecting the interference pattern in height and, thus, the offset is not important so we set $M(0)$ to an arbitrary constant.
2) In the mixed layer, $dM/dz$ is set to 0.13 $M$-units/m, a value that is consistent with the definition of a mixed layer (i.e., the potential temperature and the potential water vapor pressure are constant with respect to height) and definitions of potential refractivity and its relationship to modified refractivity provided in [14]. Furthermore, analysis of VOCAR soundings demonstrated remarkably little variability about the 0.13 $M$-units/m slope value [15].
3) Because it is upward refracting, it is suspected that the region above the capping inversion contributes to the field at beyond-line-of-sight regions, primarily through the scatter associated with fluctuations in the $M$-profile (as opposed to its slope) and that the slope itself is less important. Thus, $dM/dz$ above the inversion is set to 0.118 $M$-units/m, which is consistent with the mean value over the whole of the United States.

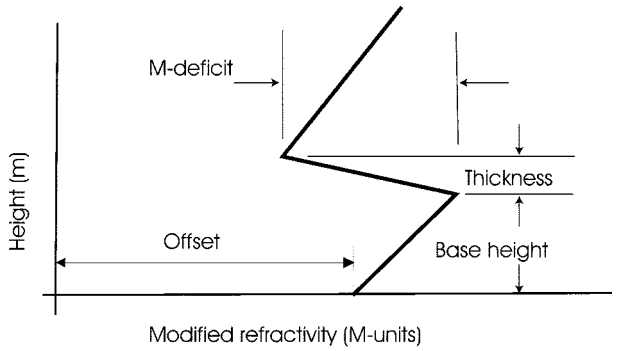


Fig. 5. Modified vertical refractivity for a trilinear profile model.

4) The length of segment above the inversion is determined by the maximum height used in the PE model.

That leaves $z_I$, $dM$, and $dz$ as the inversion variables.

While simple, the trilinear profile has been used successfully in a number of applications. An alternative to the trilinear model was sought on the expectation that a more complex model would improve estimation performance. Another possible model is the empirical orthogonal function (EOF) model [17], [18]. Based on observed refractivity profiles, a set of orthogonal functions is calculated. A given profile can then be expressed as the mean of the observed profiles plus a weighted sum of the orthogonal functions. When used in the inverse problem, an optimization algorithm will vary the relative weighting of each orthogonal function and thus change the modeled refractivity profile.

A significant problem with the EOF approach is that it is not efficient in expressing the "jump" in the profile above base height. Therefore, a variant of the EOF approach is defined where all observed profiles are shifted so that the jump in the profiles occur at the same base height $z_B$ and then the orthogonal functions are calculated. This approach is elaborated further in the Appendix and is denoted as the shifted empirical orthogonal function (SEOF) approach [15]. When used in the inverse problem, an optimization algorithm will vary the base height $z_B$ and the weighting of each orthogonal function to change the modeled refractivity profile. Simulations have shown that the SEOF representation requires about half the number of coefficients to obtain the same fit. Thus, SEOF's are preferred over EOF's.

### *B. Broad-Band Objective Functions*

The relationship between the observed complex-valued data vector $\boldsymbol{q}(\omega_l)$ on an $N$-element receive antenna array and the predicted data $\boldsymbol{p}(\boldsymbol{m}, \omega_l)$ at an angular frequency $\omega_l$ is described by the model

$$\boldsymbol{q}(\omega_l) \simeq \boldsymbol{p}(\boldsymbol{m}, \omega_l) + \boldsymbol{e}(\omega_l) \tag{1}$$

where $\boldsymbol{e}(\omega_l)$ is the error term. The predicted data is given by $\boldsymbol{p}(\boldsymbol{m}, \omega_l) = \boldsymbol{w}(\boldsymbol{m}, \omega_l)S(\omega_l)$, where the complex deterministic source signal $S(\omega_l)$ may be unknown. The transfer function $\boldsymbol{w}(\boldsymbol{m}, \omega_l)$ is obtained using an electromagnetic propagation model (here the code TPEM [4] is used) and an environmental model parameterized by the vector $\boldsymbol{m}$. In the following, $\boldsymbol{q}_l = \boldsymbol{q}(\omega_l)$, etc. is abbreviated, where $\{\omega_l | l = 1, \cdots, L\}$ is the set of frequencies processed.

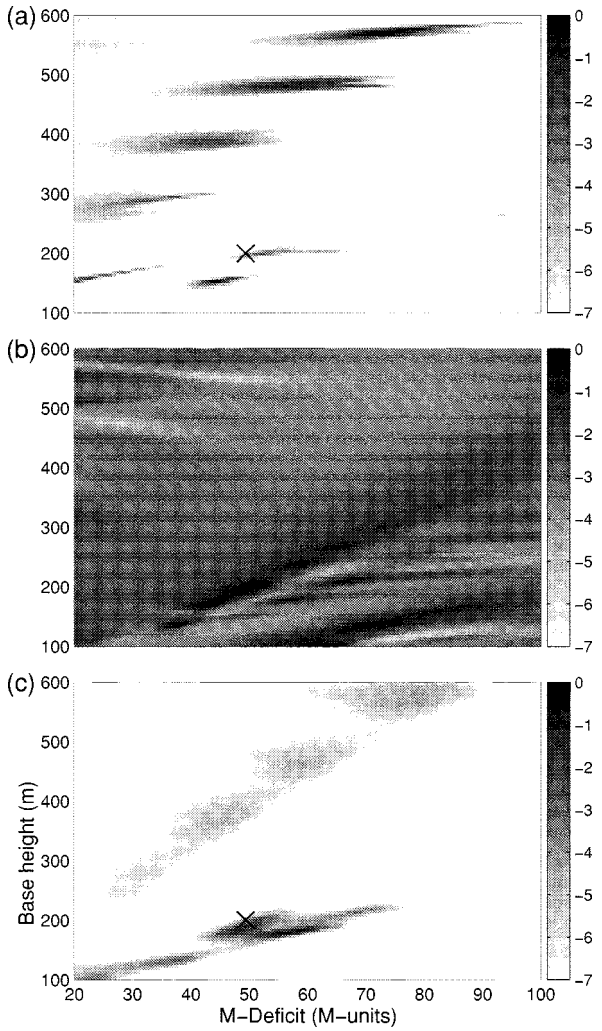


Fig. 6. Ambiguity surfaces as a function of $M$-deficit and base height in decibels relative to the minimum (dark represents a better fit). The three objective functions are (a) absolute magnitude (8); (b) relative magnitude and relative phase (6); and (c) absolute magnitude and relative phase (7). The data were generated using the surface based duct profile in Fig. 3(a) at the VOCAR frequencies. The cross indicates the value obtained by estimating the trilinear parameters directly from the profile in Fig. 3(a).

For the derivation of the objective function the errors are assumed to be additive. They stem from many sources: errors in describing the environment, errors in the forward model, instrument and measurement errors, and noise in the data. The error term is assumed complex Gaussian distributed, stationary with zero mean, and the error at each receiver is uncorrelated with a noise power $\nu_l$. Thus, the data $\boldsymbol{q}_l$ on the receiving array are also complex Gaussian distributed. For the derivation of a maximum likelihood estimate, it further is assumed that the data are uncorrelated across frequency and time. Under these assumptions, the likelihood function [19] becomes[1]

$$\mathcal{L}(\boldsymbol{m}, S_l, \nu_l) = \prod_{l=1}^{L} (\pi\nu_l)^{-N} \exp\left[-\frac{\|\boldsymbol{q}_l - \boldsymbol{w}_l(\boldsymbol{m})S_l\|^2}{\nu_l}\right]. \tag{2}$$

[1]$|\boldsymbol{v}| = (|v_1|, |v_2|, \cdots)$ and $\|\boldsymbol{v}\|^2 = \sum_i |v_i|^2$; $^T$ is transpose and $^\dagger$ is complex conjugate transpose.

Assuming that the noise powers $\nu_l, l = 1, \cdots, L$ are known and constant across frequency, the likelihood function can be further simplified to

$$\log[\mathcal{L}(\boldsymbol{m}, S_l)] \propto -\sum_{l=1}^{L} ||\boldsymbol{q}_l - \boldsymbol{w}_l(\boldsymbol{m})S_l||^2. \quad (3)$$

The maximum likelihood estimate $\hat{\boldsymbol{m}}$ for $\boldsymbol{m}$ is obtained by jointly maximizing (3) over the source signal $(S_l, \forall l)$ and the model parameter vector $\boldsymbol{m}$. The maximization with regard to $S_l$ is obtained in closed form by requiring $\partial\mathcal{L}/\partial S_l = 0$; this gives the estimate $\hat{S}_l$. Substituting this estimate into the log-likelihood function (3), the estimate $\hat{\boldsymbol{m}}$ can be obtained by minimizing

$$\phi(\boldsymbol{m}) = \sum_{l=1}^{L} ||\boldsymbol{q}_l - \boldsymbol{w}_l(\boldsymbol{m})\hat{S}_l||^2 = \sum_{l=1}^{L} \phi_l(\boldsymbol{m}) \quad (4)$$

where the objective function for each frequency $\phi_l(\boldsymbol{m})$ is introduced

$$\phi_l(\boldsymbol{m}) = ||\boldsymbol{q}_l - \boldsymbol{w}_l(\boldsymbol{m})\hat{S}_l||^2. \quad (5)$$

Depending on the *a priori* assumptions for the signal, the following maximum likelihood objective functions can be derived for each frequency component.

*1) Relative Magnitude and Relative Phase of the Field:* This is the so-called Bartlett objective function. When the receivers record the complex valued field and the complex source strength $S_l$ is unknown, the source strength then is estimated as $\hat{S}_l = \boldsymbol{w}_l^\dagger(\boldsymbol{m})\boldsymbol{q}_l/||\boldsymbol{w}_l(\boldsymbol{m})||^2$. For this objective function it is common practice to normalize it with the norm of the data $||\boldsymbol{q}_l||^2$ at each frequency. Doing this the objective function becomes

$$\phi_{l,1}(\boldsymbol{m}) = \left(1 - \frac{|\boldsymbol{w}_l^\dagger(\boldsymbol{m})\boldsymbol{q}_l|^2}{||\boldsymbol{q}_l||^2||\boldsymbol{w}_l(\boldsymbol{m})||^2}\right). \quad (6)$$

The Bartlett objective function is a weighted variation of phase over the array. It contains no information about the propagation loss from the source to the receiver. This form is often used in ocean acoustics [20], and was used in [1].

*2) Absolute Magnitude and Relative Phase of the Field:* Here, we assume the magnitude $|S_l|$ of the source is known but the phase of the source signal is unknown, otherwise the same assumptions as in Section III-B.1 are used. The closed-form solution for the source strength then is $\hat{S}_l = |S_l|\boldsymbol{w}_l^\dagger(\boldsymbol{m})\boldsymbol{q}_l/|\boldsymbol{w}_l^\dagger(\boldsymbol{m})\boldsymbol{q}_l|$. The following objective function is obtained:

$$\phi_{l,2}(\boldsymbol{m}) = ||\boldsymbol{q}_l||^2 + |S_l|^2||\boldsymbol{w}_l(\boldsymbol{m})||^2 - 2|S_l|\,|\boldsymbol{w}_l^\dagger(\boldsymbol{m})\boldsymbol{q}_l|. \quad (7)$$

This expression uses more *a priori* information about the source than the Bartlett processor (6) and differs from the magnitude only objective function in that it also utilizes the phase information. Provided that the assumptions hold and that complex data are available, this is a good alternative to the other objective functions.

*3) Absolute Magnitude of the Field:* It is here assumed that the receivers record only the magnitude of the field and the source strength $|S_l|$ is known. The complex-valued data model in (1) is then replaced with a similar one for magnitude only. It is similarly assumed that the errors are real Gaussian distributed.

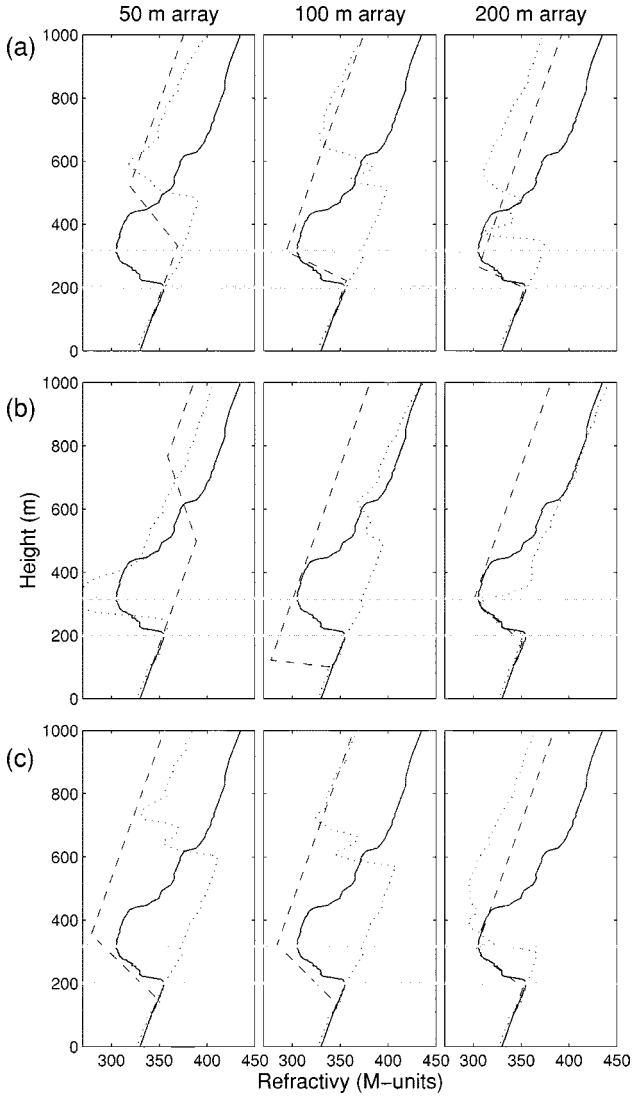


Fig. 7. Measured *surface-based duct* profile (solid line) along with matched-field estimated profiles using the trilinear model (dashed) and the SEOF model (dotted). Objective functions were (a) absolute magnitude (8); (b) relative magnitude and relative phase (6); and (c) absolute magnitude and relative phase (7). Antenna apertures were: 50, 100, and 200 m. The gray lines indicate the extend of the trapping layer, as estimated from the observed profile.

[The complex-valued (1) could also be used for deriving the objective function but this is much more complicated as the phase must be integrated out [21].] The objective function becomes

$$\begin{aligned}\phi_{l,3}(\boldsymbol{m}) &= [|\boldsymbol{q}_l| - |S_l||\boldsymbol{w}_l(\boldsymbol{m})|]^T[|\boldsymbol{q}_l| - |S_l||\boldsymbol{w}_l(\boldsymbol{m})|] \\ &= ||\boldsymbol{q}_l||^2 + |S_l|^2||\boldsymbol{w}_l(\boldsymbol{m})||^2 - 2|S_l||\boldsymbol{q}_l|^T|\boldsymbol{w}_l(\boldsymbol{m})|. \quad (8)\end{aligned}$$

Thus, only the absolute magnitude of the field across the array is optimized. This form is often used when inverting propagation loss data [22].

### C. Frequency and Spatial Diversity

The form of the objective functions in Section III-B suggests that data at more frequencies are preferable; this is usually true, with the following exceptions. First, the parameterization of the environment might be less correct for some frequencies, which will clearly have a negative effect on the estimation. An electromagnetic example is the use of frequencies above 3 GHz, where

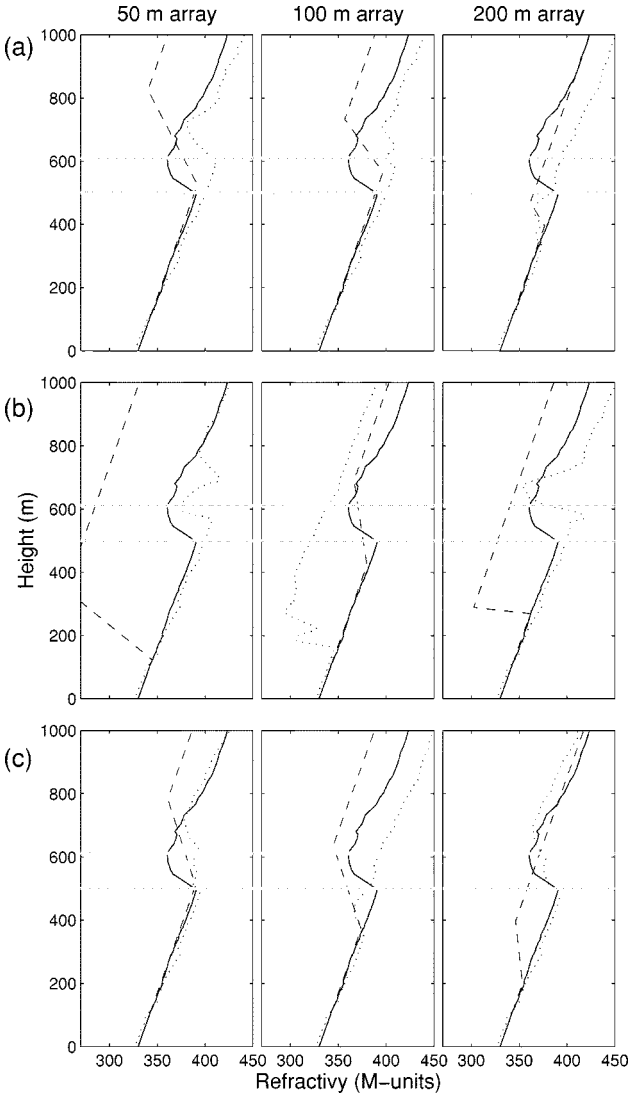


Fig. 8. Measured *elevated duct* profile (solid line) along with matched-field estimated profiles using the trilinear model (dashed), and the SEOF model (dotted). Objective functions were (a) absolute magnitude (8); (b) relative magnitude and relative phase (6); and (c) absolute magnitude and relative phase (7). Antenna apertures were: 50, 100, and 200 m. The gray lines indicate the extend of the trapping layer, as estimated from the observed profile.

the evaporation duct is most important, to estimate the trilinear parameters. Second, even if the parameterization of the environment is known precisely, emphasizing data from frequencies that are not important for the parameters being estimated can have a negative effect on the estimation. Multifrequency inversions are now becoming standard in ocean acoustics for multiparameter inversions [18] or for plotting of ambiguity functions [23]. They have found that using the field from just a few frequencies is sufficient to make the solution more stable. Naturally, the frequencies must be in a range where the numeric modeling is adequate and the objective function extract relevant features of the field.

A central question is how much of the duct needs to be sampled in height. Again, the more useful information the better. Thus, it is preferable to sample in height so that most of the energy flux of the field is sampled, this corresponds to covering the entire duct. An example is the surface-based duct coverage

TABLE II
PARAMETER SEARCH BOUNDS FOR THE TRILINEAR PROFILE MODEL

| Parameter | Lower bound | Upper bound |
|---|---|---|
| Base height (m) | 100 | 600 |
| Thickness (m) | 0 | 300 |
| M-deficit (M-units) | 0 | 100 |

diagram, Fig. 3(a), where the main interference pattern is below about 400 m (base of trapping layer). The best estimation performance is obtained if the entire space between the surface and 400 m were sampled. Clearly, sampling this entire space is difficult, but how much of the duct height needs to be sampled to obtain adequate estimation performance?

The field structure changes with frequency and this information can also be used to interfere the environmental parameters. Therefore, using several frequencies it is possible to sample the field only across a fraction of the duct height, as will be demonstrated in Section IV.

### D. Parameter Coupling

An important issue is how well parameters are resolved. The parameters also are coupled as indicated by the ambiguity surfaces in Fig. 6 where the $M$-deficit is plotted against base height for the three objective functions. The amount of coupling is dependent on the objective function, but if the base height is over estimated then the $M$-deficit also tends to be so. Using just absolute magnitude as in Fig. 6(a), several local maxima are produced. Use of relative magnitude and relative phase as in Fig. 6(b), the solution is isolated to be in the lower right part of the ambiguity surface. Using both absolute magnitude and relative phase as in Fig. 6(c), a maximum value close to the values estimated directly from the original profile is obtained.

## IV. SIMULATION RESULTS

This section presents the results of computer simulations carried out to evaluate the performance of matched-field processing for the estimation of atmospheric refractivity profiles. A simulation scenario with the following general characteristics was used.

*Source Signal*: The synthetic signal simulated an omnidirectional CW point source emitter with horizontal polarization at the three VOCAR frequencies of 143, 263, and 375 MHz. The emitter–receiver geometry was based on Path A of VOCAR, the emitter–receiver range was 132.6 km, the source height was 18.4 m. The synthetic signal data was generated using TPEM based on the emitter location, receive element locations, and refractivity profile.

*Receive Antenna Array*: The receive antenna was a vertical array containing 50 omnidirectional antenna elements and with aperture either 50, 100, or 200 m. The first receive antenna element essentially was at sea level.

*Propagation Environment*: Initially two refractivity profiles corresponding to a surface-based duct and an elevated duct were used (Fig. 3). These initial results were followed by investigating a sequence of time-varying profiles (Fig. 4).

TABLE III
PARAMETER SEARCH BOUND FOR THE SEOF PROFILE MODEL

| Parameter | Lower bound | Upper bound |
|---|---|---|
| Base height (m) | 110 | 400 |
| EOF Coefficient 1 | -1000 | 1000 |
| EOF Coefficient 2 | -300 | 300 |
| EOF Coefficient 3–4 | -200 | 200 |
| EOF Coefficient 5–14 | -60 | 60 |

*Refractivity Profile Models*: Two profile models were used—the trilinear and SEOF. The search bounds used by the estimation process are given in Table II for the trilinear model (Fig. 5) and Table III for the SEOF model.
*Objective Function*: Three objective functions as defined by (6)–(8) were used. In all cases, the objective functions were summed over the three VOCAR frequencies. The matched-field replica vectors (predicted propagation data) were generated using the TPEM propagation model.
*Optimization Parameters*: The propagation code and objective function were incorporated into the SAGA code which uses GA for optimization [24]. The GA search parameters were: parameter quantization 128 values; population size 64; reproduction size 0.5; cross-over probability 0.05; number of iterations for each population 2000; and number of populations 10. Thus, 20 000 forward modeling runs were performed for each inversion. For further information about the use of GA for parameter estimation see [16].
*CPU Run Time*: The GA computations, 20 000 forward model runs, required about 3 h of CPU time on a SUN Ultra 2/2200.

### A. Surface-Based Duct Example

The first simulation considered the surface-based duct example whose refractivity profile was illustrated in Fig. 3(a) along with the corresponding coverage diagram. This profile produces a surface-based duct up to about 300 m. Synthetic data were generated at the three VOCAR frequencies using the measured refractivity profile, using the VOCAR Path A geometry (Table I) and for each of the three receive antenna array apertures. Using the synthetic data, matched-field processing was applied to estimate the modeled refractivity profile based on the simulated measurements. Fig. 7 illustrates the inversion results for three receive array apertures, three objective functions and two refractivity profile models. On each of the plots, the measured profile is indicated by the solid line, the trilinear profile model estimate by the dashed line, and the SEOF model estimate by the dotted line. The horizontal lines indicate the location of the trapping layer.

Fig. 7(a) provides the results obtained using the absolute magnitude objective function (8). This objective function assumes that the emitter source strength is known and uses the magnitude information across the receive array. In this case, the 100- and 200-m aperture array with the trilinear refractivity model provided estimated profiles that were close to the measured profile. The base height, thickness, and $M$-deficit estimates are nearly perfect. As seen on the three panels of Fig. 7(a), the more complicated SEOF profile model did not perform well.

Fig. 7(b) illustrates the result when the objective function was Bartlett objective function (6). This objective function does not assume that the emitter source strength is known and uses the relative magnitude and phase information across the array. The 100-m aperture array correctly estimated a duct, but the height was a factor two too small. The 200-m aperture array provided good estimates with both the trilinear and SEOF profile models.

Finally, Fig. 7(c) illustrates the results for the objective function of (7). This objective function assumes that the emitter source strength is known and uses the relative phase information across the array as well as the magnitude information. In this case, fairly good estimates were obtained even with the 50-m aperture array when the trilinear profile model was used. The trilinear profile model estimates improve as the array aperture increases. When the SEOF model was used only the 200-m aperture array provided a reasonable estimate.

### B. Elevated Duct Example

The second simulation considered the elevated duct example whose refractivity profile was illustrated in Fig. 3(b) along with the corresponding coverage diagram. This profile has an elevated duct between about 200 and 600 m. Since neither the simulated emitter at 18.4 m nor the receive array elements are in the duct, it is not expected that the elevated duct profile can be estimated as well as the surface-based duct profile. However, what would be desirable is the ability to distinguish between surface and elevated ducting conditions even if the refractivity profile estimate is not very accurate.

Fig. 8 illustrates the inversion results obtained for the elevated duct profile example. As in the previous example, a wide variety of results are presented for the objective function, array aperture, and refractivity profile model options. Fig. 8(a) illustrates the results obtained using the absolute magnitude objective function (8). For this case, both the trilinear and SEOF model based estimates roughly are equivalent and clearly indicate elevated ducting conditions.

Fig. 8(b) illustrates the results obtained with the Bartlett objective function (6). The Bartlett objective function does not take into account the emitter source strength information. By the relative poor performance with this objective function, it can be noted that the elevated duct profile case requires this additional information in order to obtain reasonable profile estimates.

When the absolute magnitude and relative phase objective function (7) was used, the results were improved for both refractivity profile models, Fig. 8(c). Even the results for the 50-m aperture array with the SEOF profile model were reasonable. In this case, the 200-m aperture array with the SEOF profile model produced a very good profile estimate.

### C. Time Series Example

To gain a statistical indication of performance, time series of refractivity profiles that were calculated from radiosondes launched over a 4.5 day period during the VOCAR IOP from the R/V Point Sur are used. The 27 refractivity profiles were illustrated in Fig. 4. Note that for the first 13 profiles there exists a relatively "strong" surface-based duct with a relativity large average $M$-deficit of about 40 $M$-units and an average base-height of 200 m. Profile 14 is a transitional profile. Starting with

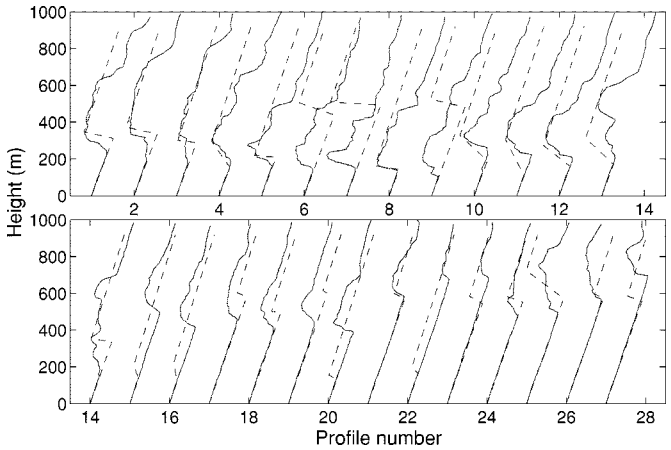


Fig. 9. Measured profiles from R/V Point Sur (solid line) along with estimated profiles (dashed line) for a *50-m aperture array.* The profiles were estimated using objective function (7) with the trilinear profile.

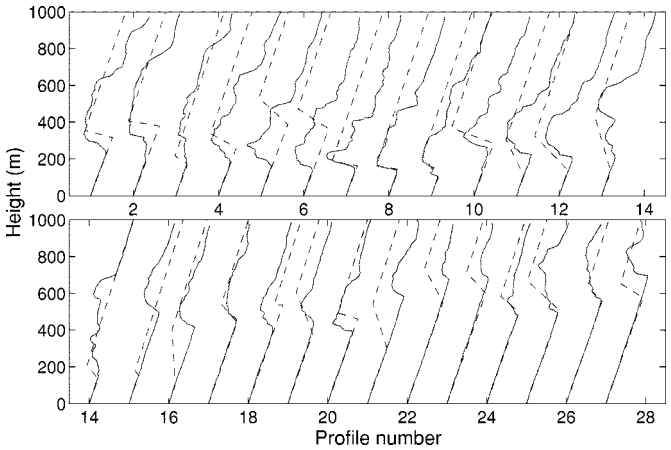


Fig. 10. Measured profiles from R/V Point Sur (solid line) along with estimated profiles (dashed line) for a*100-m aperture array.* The profiles were estimated using objective function (7) with the trilinear profile.

profile 15 there is a somewhat weaker elevated duct with an average $M$-deficit of about 20 $M$-units and average base height of about 500 m.

For this example, synthetic data were generated for each of the 27 measured refractivity profiles. Then the matched-field estimation process was carried out for each profile. Based on the results obtained for the previous two examples, it was decided that the absolute magnitude and relative phase objective function (7), combined with the trilinear profile model would be used for the analysis of the time series profiles. Both 50- and 100-m aperture arrays were used.

Fig. 9 illustrates the estimation results obtained using the 50-m aperture array. The estimated profiles (dashed lines) are plotted along with the measured profiles (solid lines). For a large percentage of the profiles, about 70%, the estimated trilinear profile model provides a relatively good fit to the measured profiles. This is a remarkable result, as only the first 50 m of the field was sampled by the receive array.

Fig. 10 illustrates the same situation except the 100-m aperture array was used. In this case, nearly all of estimated profiles are quite close to the measured profiles. In general, it looks as if the base height and $M$-deficit are being estimated accurately. In almost all cases, both the surface-based ducts and the elevated ducts were correctly identified.

Fig. 11 illustrates the result when the trilinear model parameters (base height, $M$-deficit and thickness) were extracted from the time series of measured and estimated profiles. Overall, except for the thickness parameter, the parameter estimates are quite close to those obtained from the measured profiles. As expected, the parameter estimates based on the 50-m aperture array are not as accurate as those obtained with the 100-m aperture array.

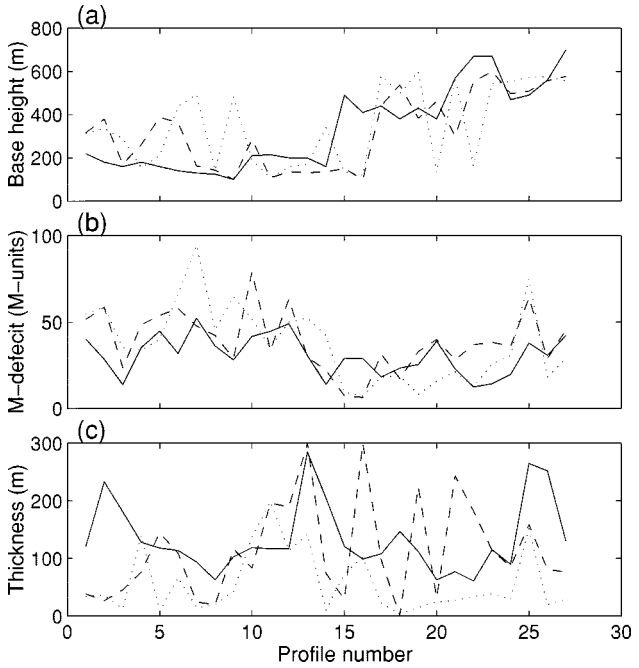


Fig. 11. Parameters for the trilinear model versus profile number (a) base height; (b) $M$-deficit; and (c) thickness for the R/V Point Sur time series. Parameters based on the measured profiles are indicated by the solid lines. Parameter estimates based on Fig. 10 [(7) with 100-m aperture array] are indicated by the dashed lines. Parameter estimates based on Fig. 9 [(7) with 50-m aperture array] are indicated by the dotted lines.

### *D. Propagation Predictions*

As the final measure of performance, propagation loss predictions were calculated. Fig. 12 illustrates a result for the surface-based and elevated duct examples. Fig. 12(a) illustrates a coverage diagram based on the surface-based duct refractivity profile estimated using the 100-m aperture array, the trilinear profile model, and the absolute magnitude and relative phase objective function (7). The estimated profile is plotted along with the measured profile on the left side of the figure. This result should be compared with Fig. 3(a), which was computed based on the measured surface-based duct profile. It can be seen that the two coverage diagrams are quite similar. Both have a "beam" of energy that is refracted by the trapping layer at about 50 km and reflected off the surface at about 100 km. The elevated duct result in Fig. 12(b) should be compared with that of Fig. 3(b). In this case, the two coverage diagrams are also quite similar. But, the one based on the estimated profile predicts a larger propagation loss at lower elevations and longer ranges than that based on the measured profile.

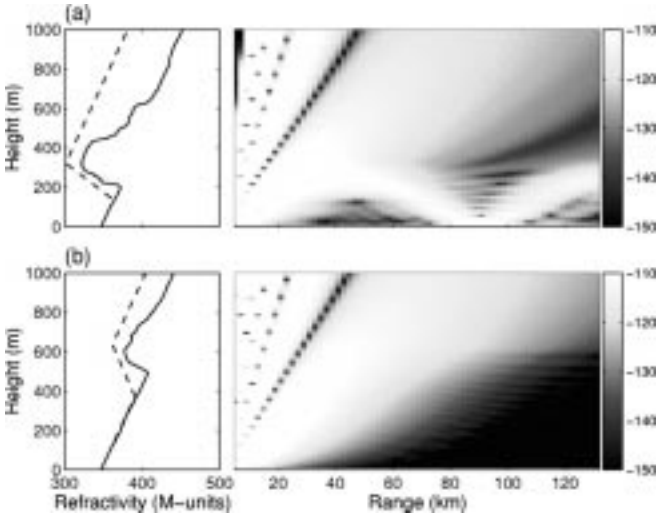


Fig. 12. Refractivity profiles, measured (solid) and estimated (dashed), and corresponding coverage diagrams based on estimated refractivity profiles at 375 MHz for (a) surface-based duct and (b) elevated duct. The estimated profiles are based on using the 100-m aperture array, the trilinear profile model, and the absolute magnitude and relative phase objective function (7).

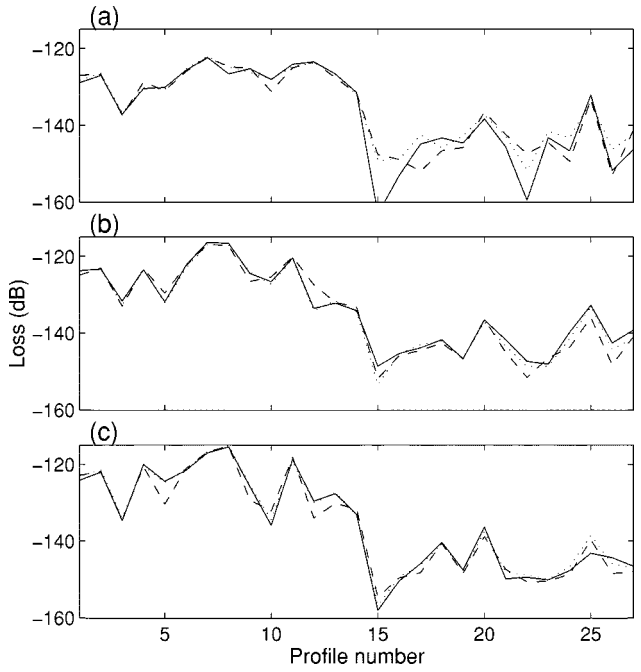


Fig. 13. Propagation loss versus profile number based on the R/V Point Sur measured profiles (solid line), the Fig. 10 trilinear parameter estimates (dashed) [(7) with 100-m aperture array], and the Fig. 9 trilinear parameter estimates (dotted) [(7) with 50-m aperture array] for three frequencies: (a) 143; (b) 263; and (c) 375 MHz. The emitter height was 18.4 m, the receiver height 30.5 m, and the emitter–receiver range 132.6 km.

The propagation loss at a single point was calculated for the three refractivity profile time series (measured, estimate based on the 50-m aperture array, and estimate based on the 100-m aperture array) at the three VOCAR frequencies Fig. 13. The solid line illustrates the propagation loss as predicted based on the trilinear parameters estimated directly from the measured profiles. The dashed line illustrates the predicted loss based on the trilinear parameters estimated from the 100-m aperture array with the absolute magnitude and relative phase objective function (7). At all three frequencies these loss predictions closely resemble the ones based on the measured profiles. The dotted line illustrates the loss based on the trilinear parameters estimated using the 50-m aperture array. The results based on the 50-m aperture array are only marginally degraded.

## V. Conclusions

The focus of this paper has been on quantifying the performance of matched-field processing methods for the remote sensing of refractivity profile structure in the lower troposphere using simulated propagation data from a single transmitter to a vertical array of receivers. The performance was evaluated as a function of: 1) the aperture of the receive array (50, 100, and 200 m); 2) the refractivity profile model (trilinear and SEOF); and 3) the objective function used in the optimization (absolute magnitude, relative magnitude and phase, and absolute magnitude and relative phase). Refractivity profile estimation results were presented for a surface-based duct example, an elevated duct example and a sequence of time-varying refractivity profiles. The refractivity profiles used in the simulations were obtained from radiosonde measurements collected during the VOCAR experiment off the coast of southern California. The main simulation results are as follows.

1) *Performance of the Refractivity Profile Models:* The surprising result was the very robust performance of the trilinear refractivity profile model. The heuristic trilinear model performed better than the far more complex SEOF model for the surface-based duct example. To some degree, the SEOF model outperformed the trilinear model for the more difficult elevated duct example. These results are not conclusive in that at different frequencies or geometries, variability in the refractivity structure may require the more complex SEOF model.
2) *Surface-Based Duct:* For the surface-based duct example, good estimation results were obtained using the 50-m aperture array with the absolute magnitude and relative phase objective function (7) and trilinear profile model. Near perfect results were obtained with all three objective functions (6)–(8) when the 200-m aperture array was used with the trilinear profile model.
3) *Elevated Duct:* For the elevated duct example, the profile estimation results were less impressive. Essentially, a good estimate was obtained for only one case, the 200-m aperture array with the absolute magnitude and relative phase objective function (7) and SEOF profile model. The SEOF profile model seemed to outperform the trilinear profile model for this case.
4) *Time Series:* The results obtained for the R/V Point Sur profile time series were very impressive. Using the 100-m aperture array and the absolute magnitude and relative phase objective function (7), most of the 27 profiles were well estimated. The trilinear parameter estimate results of Fig. 11 were equally impressive. The estimates of the three parameters, except for thickness, closely follow the parameters derived from the measured profiles.

5) *Propagation Predictions:* The propagation predictions in Fig. 13 at the three VOCAR frequencies based on the estimated trilinear profile parameters tracked very closely those based on the measured profiles.

Based on the limited simulations presented here, it is demonstrated that remote sensing of time-varying refractivity profile structure is feasible using an array with aperture 50–100 m, a simple parameterization of the refractivity profile (trilinear), and a sophisticated objective function (absolute magnitude and relative phase across the array). The refractivity profile estimates for surface-based duct profiles were very good while those for elevated ducts were less accurate. However, the inversion process clearly was able to distinguish between surface-based and elevated ducting conditions. Furthermore, the results showed that the estimated refractivity profiles were of sufficient quality to provide propagation loss predictions at all frequencies very close to those generated from trilinear versions of the original profiles.

## APPENDIX
## SHIFTED EMPIRICAL ORTHOGONAL FUNCTION (SEOF) REFRACTIVITY PROFILE MODEL

An observed refractivity profile $r(z)$, where $z$ is the height (assumed to be discrete values), may be modeled as $\hat{r}(z)$

$$r(z) \approx \hat{r}(z;\, c_1, \cdots, c_K) = \overline{r}(z) + \sum_{k=1}^{K} c_k v_k(z) \qquad (9)$$

where

| | |
|---|---|
| $\overline{r}(z)$ | mean profile; |
| the $\{v_k\}$ | empirical orthogonal functions (EOF's) developed from historical data; |
| the $\{c_k\}$ | corresponding coefficients. |

When used in the inverse medium problem, an optimization algorithm will vary the coefficients $c_1, \cdots, c_K$ to find the estimated refractivity profile that provides the best match between the predicted and observed propagation data.

There are three potential problems when using EOF's for refractivity modeling in the electromagnetic inverse medium problem. First, many coefficients may be required to adequately represent a profile (experience indicates that 6–10 are typically required to adequately fit the VOCAR soundings); second, nonphysical profiles may result; and third EOF coefficients do not easily transform to meteorologically meaningful parameters.

Since the thickness of the trapping layer is on the order of 100–200 m and the base height can vary over 500 m, it is reasonable to expect that a more compact parameterization could be obtained by using EOF's that are referenced to the base height. A second advantage is that in this form the base height, which is a meaningful meteorological parameter, is an explicit parameter. The shifted EOF (SEOF) parameterization is now described.

1) Each profile $r_i(z)$ is shifted such that the height is referenced to the trapping layer base height $z_{B,i}$ for that profile

$$r_i^S(z) = r_i(z - z_{B,i}) \qquad (10)$$

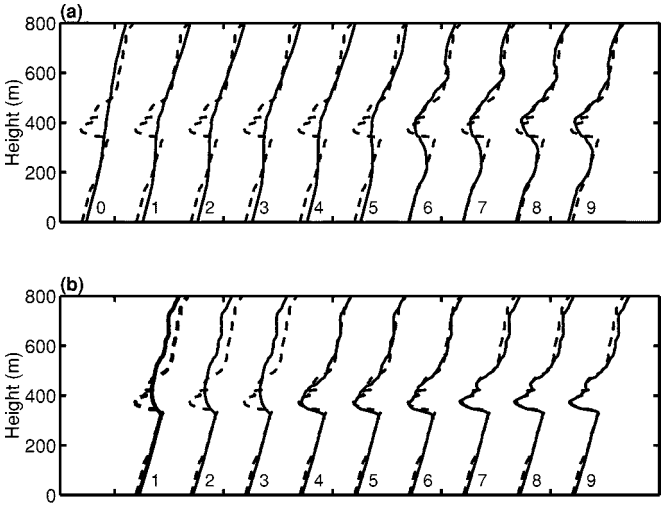


Fig. 14. Example of (a) EOF and (b) SEOF profiles (solid lines) for increasing numbers of coefficients. The SEOF's provide a better fit to the real profile (dashed lines) using four parameters than the EOF's using nine parameters.

where $r$ is the modified refractivity and the superscript $S$ denotes that the profile was shifted.

2) Let there be $N$ shifted refractivity profiles, each profile is a column vector $\boldsymbol{r}_i^S$ of length $P$. The mean profile vector $\overline{\boldsymbol{r}}^S$ and the $P \times P$ covariance matrix $\boldsymbol{R}_r^S$ are calculated

$$\overline{\boldsymbol{r}}^S = \langle \boldsymbol{r}^S \rangle$$
$$\boldsymbol{R}_r^S = \langle (\boldsymbol{r}^S - \overline{\boldsymbol{r}}^S)(\boldsymbol{r}^S - \overline{\boldsymbol{r}}^S)^T \rangle. \qquad (11)$$

The notation $\langle\ \rangle$ indicates an ensemble average, the superscript $T$ indicates transpose.

3) The eigenvectors $\boldsymbol{v}_k^S(z)$ of $\boldsymbol{R}_r^S$ are EOF's spanning the set of shifted refractivity profiles used to generate $\boldsymbol{R}_r^S$. Let the eigenvalues $\lambda_k^S$ of $\boldsymbol{R}_r^S$ and corresponding eigenvectors be arranged in descending order $\lambda_1^S > \lambda_2^S > \cdots > \lambda_P^S$. A linear combination of $K$ orthogonal functions based on the first $K$ eigenvectors yields a minimum mean-squared error representation

$$\hat{r}_i(z;\, z_{B,i}, c_1, \cdots, c_K) = \overline{r}^S(z + z_{B,i}) + \sum_{k=1}^{K} c_k v_k^S(z + z_{B,i}) \qquad (12)$$

where $K < P$.

4) An optimization algorithm will vary the base height $z_{B,i}$ and the coefficients $c_1, \cdots, c_K$ to obtain a refractivity profile estimate.

The advantage of using the SEOF representation relative to the EOF representation is illustrated in Fig. 14. For this profile, the SEOF representation provides a better fit using four coefficients than the EOF representation when using nine coefficients. Simulations with other profiles have shown that the SEOF representation requires about half the number of EOF coefficients to obtain the same fit.

In addition to the above general discussion, the following additional constraints were applied to the implementation used herein. Only the region from 100 m below to 200 m above the base height was estimated by varying the coefficients in (12) (the regions below and above were modeled using realizations based on second-order statistics over the entire set of soundings).

## ACKNOWLEDGMENT

The authors would like to thank R. Paulus of the SPAWAR Systems Center, San Diego, CA, for carefully collecting and supplying the VOCAR radiosonde data.

## REFERENCES

[1] D. F. Gingras, P. Gerstoft, and N. L. Gerr, "Electromagnetic matched field processing: Basic concepts and tropospheric simulations," *IEEE Trans. Antennas Propagat.*, vol. 42, pp. 1305–1316, Oct. 1997.

[2] G. D. Dockery, "Modeling electromagnetic wave propagation in the troposphere using the parabolic equation," *IEEE Trans. Antennas Propagat.*, vol. 36, pp. 1464–1470, Oct. 1988.

[3] H. V. Hitney, "Hybrid ray optics and parabolic equation methods for radar propagation modeling," in *Proc. Inst. Elect. Eng. Radar '92 Conf.*, Brighton, U.K., Oct. 1992, pp. 58–61.

[4] A. E. Barrios, "A terrain parabolic equation model for propagation in the troposphere," *IEEE Trans. Antennas Propagat.*, vol. 42, pp. 90–98, Jan. 1994.

[5] M. F. Levy, "Horizontal parabolic equation solution of radiowave propagation problems on large domain," *IEEE Trans. Antennas Propagat.*, vol. 43, pp. 137–143, Feb. 1995.

[6] J. H. Richter, "Variability and sensing of the coastal environment," in *AGARD Conf. Proc. CP-567*, Bremerhaven, Germany, Sept. 1994, pp. 1.1–1.3.

[7] H. V. Hitney, "Remote sensing of refractivity structure by direct measurements at UHF," in *AGARD Conf. Proc. CP-502*, Cesme, Turkey, Feb. 1992, 1, pp. 1.1–1.5.

[8] D. Boyer, G. Gentry, J. Stapleton, and J. Cook, "Using remote refractivity sensing to predict tropospheric refractivity from measurements of propagation," in *Proc. AGARD SPP Symp. Remote Sensing: Valuable Source Inform.*, Toulouse, France, Apr. 22–25, 1996, pp. 16.1–16.13.

[9] J. Tabrikian and J. Krolik, "Theoretical performance limits on tropospheric refractivity estimation using point-to-point microwave measurements," *IEEE Trans. Antennas Propagat.*, vol. 47, pp. 1727–1734, Nov. 1999.

[10] L. T. Rogers, "Likelihood estimation of tropospheric duct parameters from horizontal propagation measurements," *Radio Sci.*, vol. 32, pp. 79–92, Jan./Feb. 1997.

[11] K. D. Anderson, "Tropospheric refractivity profiles inferred from low elevation angle measurements of Global Positioning System (GPS) signals," in *AGARD Conf. Proc. CP-567*, Bremerhaven, Germany, Sept. 1994, pp. 2.1–2.7.

[12] R. A. Paulus, "VOCAR: An experiment in the variability of coastal atmospheric refractivity," in *Proc. Int. Geosci. Remote Sensing Symp.*, vol. I. Pasadena, CA, Aug. 1994, pp. 386–388.

[13] S. D. Burk and W. T. Thompson, "Mesoscale modeling of summertime refractive conditions in the southern California bight," *J. Appl. Meteor.*, vol. 36, pp. 22–31, Jan. 1997.

[14] E. E. Gossard and R. G. Strauch, *Radar Observations of Clear Air and Clouds*. Amsterdam, The Netherlands: Elsevier, 1983.

[15] L. T. Rogers, "Demonstration of an efficient boundary layer parameterization for unbiased propagation estimation," *Radio Sci.*, vol. 33, no. 6, pp. 1599–1608, 1998.

[16] P. Gerstoft, "Inversion of seismoacoustic data using GA and a posteriori probability distributions," *J. Acoust. Soc. Amer.*, vol. 95, pp. 770–782, Feb. 1994.

[17] L. R. LeBlanc and F. H. Middleton, "An underwater acoustic sound velocity data model," *J. Acoust. Soc. Amer.*, vol. 67, pp. 2055–2062, June 1980.

[18] P. Gerstoft and D. F. Gingras, "Parameter estimation using multifrequency range-dependent acoustic data in shallow water," *J. Acoust. Soc. Amer.*, vol. 99, pp. 2839–2850, May 1996.

[19] D. H. Johnson and D. E. Dudgeon, *Array Signal Processing*. Englewood Cliffs, NJ: Prentice-Hall, 1993.

[20] D. F. Gingras and P. Gerstoft, "Inversion for geometric and geoacoustic parameters in shallow water: Experimental results," *J. Acoust. Soc. Amer.*, vol. 97, pp. 3589–3598, June 1995.

[21] C. F. Mecklenbräuker and P. Gerstoft, "Uncertainties in geoacoustic parameter estimates," J. Computat. Acoust., to be published.

[22] L. T. Rogers, "Effects of the variability of atmospheric refractivity on propagation estimates," *IEEE Trans. Antennas Propagat.*, vol. 44, pp. 460–465, Apr. 1996.

[23] N. O. Booth, P. A. Baxley, J. A. Rice, P. W. Schey, W. S. Hodgkiss, G. L. D'Spain, and J. J. Murray, "Source localization with broad-band matched-field processing in shallow water," *IEEE J. Ocean. Eng.*, vol. 21, pp. 402–412, Oct. 1996.

[24] P. Gerstoft, "SAGA Users guide 2.0, an inversion sofware package," SACLANT Undersea Research Centre, SM-333, 1997.

**Peter Gerstoft** received the M.Sc. and the Ph.D. degrees from the Technical University of Denmark, Lyngby, Denmark, in 1983 and 1986, respectively, and the M.Sc. degree from the University of Western Ontario, London, Canada, in 1984.

From 1987 to 1992, he was employed at Ødegaard and Danneskiold-Samsøe, Copenhagen, Denmark, working on forward modeling and inversion for seismic exploration. From 1989 to 1990 he was a Visiting Scientist at the Massachusetts Institute of Technology, Cambridge, and at Woods Hole Oceanographic Institute, Cape Cod, MA. From 1992 to 1997 he was Senior Scientist at SACLANT Undersea Research Centre, La Spezia, Italy, where he developed the SAGA inversion code, which is used for ocean acoustic and electromagnetic signals. From 1997 to 1999 he was with Marine Physical Laboratory, University of California, San Diego. Since 1999 he has been with the Comprehensive Nuclear Test-Ban Treaty Organization, Vienna, Austria, where he is doing hydro-acoustic modeling and inversion. His research interests include global optimization, modeling and inversion of acoustic, and elastic and electromagnetic signals.

**Donald F. Gingras** (S'68–M'68) received the B.S. degree from San Diego State University, San Diego, CA, in 1968, the M.S. degree from Northeastern University, Boston, MA, in 1971, and the Ph.D. degree from the University of California, San Diego in 1986, all in electrical engineering.

From 1968 to 1971, he was a Sonar Design Engineer with Raytheon at the Submarine Signal Division, Portsmouth RI. From 1971 to 1990 he worked in array signal processing at the Naval Command Control and Ocean Surveillance Center, San Diego, CA. From 1990 to 1995 he led the Signal Processing Group at the SACLANT Undersea Research Centre, La Spezia, Italy. In 1996 he joined the Communications and Information Systems Department at the Space and Naval Warfare Systems Center, San Diego, CA. His current research interests include matched-field processing, propagation modeling, integrated services wireless networks, and multiple access protocols.

**L. Ted Rogers** was born in Miami, FL, on February 14, 1954. He received the B.S. degree in engineering sciences from the University of Florida, Gainesville, in 1983, and the M.S. degree in applied mathematics from San Diego State University, San Diego, CA, in 1990.

From 1983 until 1988, he served as a Surface Warfare Officer in the U.S. Navy. Since 1990 he has been employed by what is currently called the Space and Naval Warfare Systems Center, San Diego, CA. His primary research interest is in improving estimation of the refractivity structure associated with the marine atmospheric boundary layer through combining *in situ* and remotely sensed observation with data from numerical weather prediction models.

**William S. Hodgkiss** (S'68–M'75) was born in Bellefonte, PA, on August 20, 1950. He received the B.S.E.E. degree from Bucknell University, Lewisburg, PA, in 1972, and the M.S. and Ph.D. degrees in electrical engineering from Duke University, Durham, NC, in 1973 and 1975, respectively.

From 1975 to 1977, he worked with the Naval Ocean Systems Center, San Diego, CA. From 1977 to 1978 he was a Faculty Member in the Electrical Engineering Department, Bucknell University, Lewisburg, PA. Since 1978 he has been a member of the faculty of the Scripps Institution of Oceanography, University of California, San Diego, and on the staff of the Marine Physical Laboratory, where he is currently Deputy Director. He is the Applied Ocean Science Curricular Group Coordinator, Graduate Department of the Scripps Institution of Oceanography. His present research interests are in the areas of adaptive array processing, propagation modeling, and environmental inversions with applications of these to underwater acoustics and electromagnetic wave propagation.

Dr. Hodgkiss is a fellow of the Acoustical Society of America.